Check for updates

Urea-assisted synthesis of carbon-doped BiNbO$_4$ with oxygen vacancies and visible light photocatalytic applications†

Andrei Lebedev,‡[a] P. Vishakha T. Weerasinghe,‡[a] Franklin Anariba,[ab] Xu Li,[cd] Debbie Seng Hwee Leng[c] and Ping Wu [ID] *[a]

Although carbon doping in simple metal oxides like TiO$_2$ and ZnO has been proven to increase photocatalytic dye degradation in visible light, it's unclear if carbon doping in complex BiNbO$_4$ would have the same effect. For the first time, carbon doped BiNbO$_4$ (U-BiNbO$_4$) has been synthesized with urea as the carbon source utilizing a simple sol–gel process. The creation of oxygen vacancies and their energy levels in BiNbO$_4$'s electronic band structure are controlled by the decomposition of urea. X-Ray diffraction (XRD), X-ray photoelectron spectroscopy (XPS), and carrier scavenging tests verified the presence of surface oxygen vacancies and carbon doping. Both pure BiNbO$_4$ and U-BiNbO$_4$ are multi-crystalline structures with orthorhombic and triclinic phases. When compared to pure BiNbO$_4$, U-BiNbO$_4$ degraded cationic methylene blue (MB, 75.7 ± 3.5%) and brilliant green dyes (BG, 86.3 3.5%) more efficiently. The creation of carbon modulated oxygen vacancies and the lowering of the bandgap (from 3.19 eV to 2.95 eV for BiNbO$_4$ and U-BiNbO$_4$) were also postulated as dye degradation mechanisms. By employing a synthesis method of alternate low- and high-oxygen partial pressures, this novel process might be exploited to construct high-performance Bi-based photocatalysts.

Introduction

Photocatalysis as a technology has attracted attention for the degradation of organic and inorganic pollutants, air purification and applications in self-cleaning surfaces. Since the pioneering discovery in 1972, titanium dioxide (TiO$_2$) has been one of the most promising materials because of its low cost, chemical stability, non-toxicity and robust performance. However, the main drawback is associated with its wide band gap (3.2 eV) and its ability to absorb only UV light.[1] In order to overcome this issue, new promising materials have been developed to satisfy the demand in efficient visible light utilization. Among others, BiNbO$_4$ has been recognized and fabricated in a number of studies.[2–7] The experimental band gap of BiNbO$_4$ is 3.0 eV, which

is smaller than that for TiO$_2$, but still wide for efficient visible light absorption. In order to reduce the band gap non-metal doping has been proposed and effectively utilized to prepare visible-light-sensitive catalysts. For instance, a carbon (C) doping agent was successfully introduced in a crystal lattice in a number of works where urea, oleylamine, sucrose, *etc.* were used as a source of C.[8–14] Dyes have been efficiently used as prototyping pollutants. There are very few manuscripts published on the dye degradation of BiNbO$_4$. A comparison of the dye degradation performances by BiNbO$_4$ are summarized in Table 1. It can be concluded that doped BiNbO$_4$ shows a higher degradation rate compared to pristine BiNbO$_4$ under the same experimental conditions. Although not exhaustive, it can be seen that only one paper was released on methylene blue (MB) degradation (240 min) and no papers were published on brilliant green (BG) degradation.

Previously, by DFT calculations[15] and by hands-on experiments to prepare C-doped TiO$_2$,[16] C-doped SnO$_2$[17] and C-doped ZnO,[18] it was shown that under oxygen-poor conditions oxygen vacancies are stabilized. However, under oxygen-rich conditions, the site occupancy of carbon is more complicated which depends on the redox potentials of the cations in the semiconductor. For example, for C-doped TiO$_2$ carbon goes to the metal site (interstitial and substitutional).[15] Conversely, for p-type C-doped ZnO the most stable structure is a C–O cluster.[19] It was also shown that carbon in C-doped mono-clinic BiVO$_4$ does not lead to oxygen substitution (by carbon).[20] Urea is a low-cost and

[a] *Entropic Interface Group, Engineering Product Development, Singapore University of Technology and Design, Singapore. E-mail: wuping@sutd.edu.sg*

[b] *Anariba Brands Group, Science, Mathematics and Technology, affiliated to Engineering Product Development, Singapore University of Technology and Design, Singapore*

[c] *Institute of Materials Research and Engineering, Agency for Science, Technology and Research (A*STAR), Singapore*

[d] *Institute of Sustainability for Chemicals, Energy and Environment, Agency for Science, Technology and Research (A*STAR), Singapore, Singapore*

† Electronic supplementary information (ESI) available. See DOI: https://doi.org/10.1039/d2ma00585a

‡ These authors contributed equally.

Table 1 The literature overview of the doped-BiNbO$_4$ degradation performance towards cationic and anionic dyes

Material	Dopant	Light intensity	Catalyst amount	Dye type	Dye mass	Degradation time	Total degradation percentage (%)
BiNbO$_4$, Ag$_3$PO$_4$/BiNbO$_4$[24]	Ag$_3$PO$_4$	350 W/xenon lamp	15 mg	RhB	20 mg L^{-1}	60 min	14.9, 98.8
BiNbO$_4$, Ag/Ag$_2$O/BiNbO$_4$[25]	Ag/Ag$_2$O	48 W/100 mW cm^{-2}	15 mg	MB, RhB, AR1	1 g L^{-1}	MB: 240 min, RhB: 240 min, AR1 : 25 min	36.5, 84.2, 5.9, 55.6, 0, 88.3
BiNbO$_4$, C$_3$N$_4$/BiNbO$_4$[26]	C$_3$N$_4$	300 W/xenon lamp	15 mg	RhB	10 mg L^{-1}	40 min	25.1, 100.0

abundant material widely available in industry. It is an active molecular precursor produced by thermal treatment which can be utilized to form graphitic carbon nitride (g-C$_3$N$_4$). As a result of thermal decomposition, urea is converted to by-products such as cyanuric acid and ammonia gas. Therefore, urea may be a potential precursor for the solid state synthesis of C-doped BiNbO$_4$.[21–23] By simultaneously applying oxygen-rich and oxygen-deficient conditions, which originate from the thermal decomposition of urea, we fabricated carbon-doped BiNbO$_4$ (referred to throughout the text as U-BiNbO$_4$). The enhanced presence of C and oxygen vacancies was confirmed by X-ray photo-electron spectroscopy (XPS). The photocatalytic properties of pristine BiNbO$_4$ and U-BiNbO$_4$ were investigated toward the visible-light degradation of cationic MB and BG dyes. Electron, hole, and •OH scavenging experiments were performed and a mechanism of dye degradation was proposed based on (i) reduced band gap and (ii) C and oxygen vacancies.

Experimental

Schematics of the annealing process with a combination of high- and low-oxygen partial pressure is shown in Fig. 1 (panel A). The unique synthesis method included a tube furnace unsealed from one side and connected to an ammonia sensor on the other side to monitor the concentration of gaseous ammonia (NH$_3$), which is shown in Fig. 1 (panel B). The material was annealed at 700 °C with a heating rate of 2 degrees per min, which allowed us to measure the amount of produced ammonia. The particles were calcined at 700 °C with a heating rate of 2 degrees per min. The largest presence of ammonia was recorded at 300–400 °C (40–50 ppm), corresponding to oxygen deficient conditions. For other experiments, the amount of produced ammonia was low (below 5 ppm), which corresponds to oxygen-rich conditions (Fig. 1, panel C). As a result of the unique synthesis process, oxygen vacancies are formed, which are controlled by an oxygen-poor atmosphere.

Preparation

Reagents

Bismuth nitrate pentahydrate (Bi(NO$_3$)$_3$·5H$_2$O, 98%, Sigma-Aldrich) and niobium pentachloride (NbCl$_5$, 99%, Sigma-Aldrich) were employed as precursors to provide bismuth and niobium sources, respectively. Nitric acid (HNO$_3$, 70%, Sigma-Aldrich) and ethanol (C$_2$H$_5$OH, 96%, Sigma-Aldrich) were purchased and used as
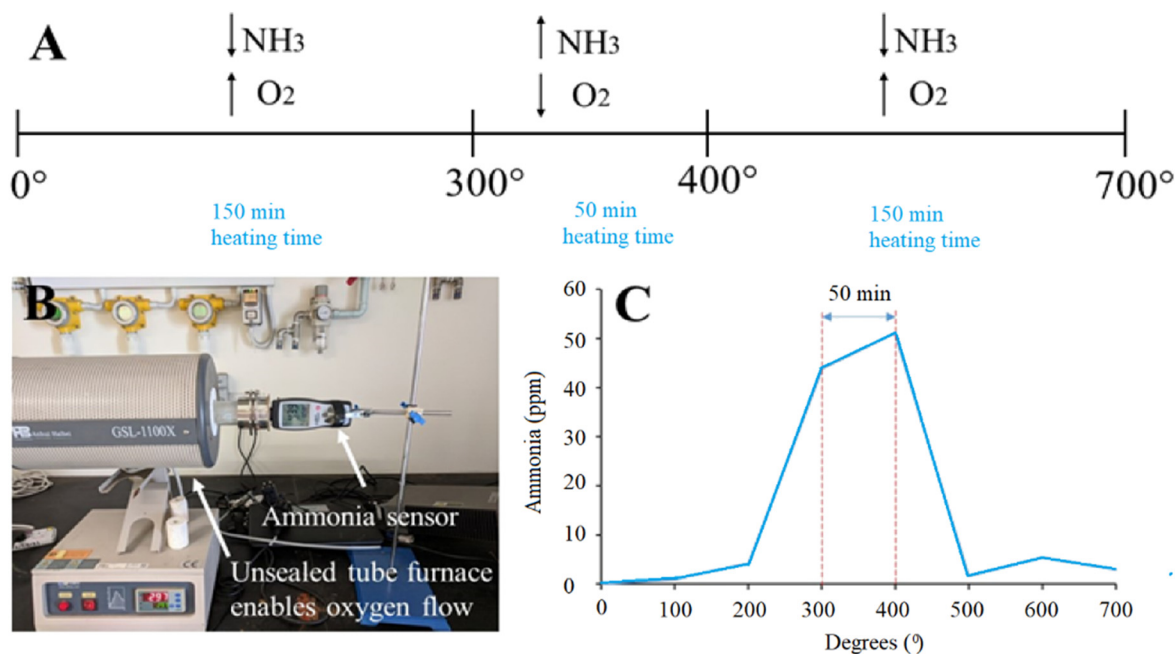
Fig. 1 (A) Schematic of the annealing process of U-BiNbO$_4$ in the tube furnace. Oxygen-poor conditions were applied between 300−400 °C, and oxygen-rich conditions were maintained below 300 °C and above 400 °C, respectively. (B) Set up with a tube furnace and ammonia sensor. The tube furnace is unsealed from one side to allow free oxygen flow. (C) A graph showing the recorded ammonia concentration (ppm) *vs.* annealing temperature (°C).

solvents. Urea (CH_4N_2O, 98%, M_w = 60.06) was purchased from Sigma-Aldrich. Ethylenediaminetetraacetic acid ($C_{10}H_{16}N_2O_8$, 98%, Sigma-Aldrich), isopropanol (C_3H_8O, 99.5%, Sigma-Aldrich) and *p*-benzoquinone ($C_6H_4O_2$, 98%, Sigma-Aldrich) were purchased as scavengers for holes, $^\bullet$OH radicals and electrons, respectively. Methylene Blue ($C_{16}H_{18}ClN_3S$, dye content 82%) and Brilliant Green ($C_{27}H_{33}N_2HO_4S$, dye content 95%) were also purchased from Sigma-Aldrich and used as prototyping pollutants. Deionized water (DI, 50 KΩ) was used throughout all experiments.

BiNbO₄ nanoparticles (NPs)

BiNbO₄ particles were synthesized by using a sol–gel method. First, 1.14 g of bismuth nitrate pentahydrate and 0.64 g of niobium chloride were separately mixed with 10 mL of ethanol each under strong magnetic stirring (solutions A and B, respectively). This was followed by the heating of solution A at 100 °C for 60 min and solution B at 70 °C for 30 min, respectively. Second, both solutions were mixed together and 0.5 mL of nitric acid was added to the mixture dropwise to make the solution precipitate (solution C). Third, the as-prepared solution C was continuously stirred for 30 min and kept in an oven at 90 °C for 24 hours until it dried. Finally, the dried material was placed in an alumina crucible and annealed in a tube furnace. Then, it was heated to 700 °C at a rate of 2 °C min^{-1} and annealed for 60 min at 700 °C.

U-BiNbO₄ catalyst

The U-BiNbO₄ composite was prepared by using the same pathway as BiNbO₄ with the addition of the following steps. Urea (2 g) was dissolved separately in 10 mL of ethanol (20 °C) as a source of carbon (urea has a solubility in ethanol of 100 g L^{-1}) and added into solution C. After 60 min of stirring, the solution was stored in an oven at 90 °C for 24 hours to dry. At the final step it was annealed in a tube furnace at 700 °C for 60 min at a heating rate of 2 °C min^{-1}.

Instrumentation and characterization

A Prizmatix Ultra High Power LED lamp and Techno Digm UVR 400/600 lamp were used for photo-degradation tests as sources of visible and UV light, respectively. X-Ray diffraction (XRD) tests were performed in a Bruker D8 Advance X-ray diffractometer with Cu Kα radiation of 0.154 nm wavelength to evaluate the powder's composition and phase. The scanning angle was set from 20° to 35°. UV-Vis absorbance measurements were carried out and collected by using a PG Instruments TIIO + UV-Vis spectrophotometer. Particle size and the corresponding morphology were evaluated by scanning electron microscope (SEM) (JEOL JSM-7600F) coupled with an energy dispersive X-ray spectrum (EDS). X-Ray photoelectron spectroscopy (XPS) tests were performed using a Thermo Fischer Scientific Theta Probe system. Using a micro-Raman device (Renishaw Raman spectrometer) and a He–Ne laser, RL633 (633 nm, 1.5 m diameter spot size), micro-Raman scattering tests were carried out in the spectral region of 50 to 1000 cm^{-1}. The annealing of the powder was performed in a tube furnace (Anhui Haibei GSL-1100X) and the light intensity was recorded

using an Optical Power Meter PM100D from Thorlabs. The amount of gaseous ammonia was measured using an XIN Air Quality Monitor Meter.

Photocatalytic performance test

The photocatalytic performance of pristine BiNbO₄ and U-BiNbO₄ oxides was investigated by photocatalytic degradation of MB and BG dyes under visible irradiation. The Prizmatix Ultra High Power LED lamp was used as a visible light source. The light intensity was set at 100 mW cm^{-2}. The experimental conditions were as follows: 15 mg of the photocatalyst was dispersed in 15 mL of a dye aqueous solution to reach a concentration of 1 g L^{-1} and the suspension was sonicated for 60 min. Before exposure to visible light the suspension was stirred for 30 min under dark conditions to reach adsorption–desorption equilibrium. Subsequently, the solution was transferred into 1.5 mL tubes and a photocatalytic reaction was initiated. The visible light exposure was set to 240 min. Every 60 min the suspension was collected and transferred into a UV-Vis cuvette. Finally, the UV-Vis absorption response was recorded.

Results and discussion

Characterization of the photocatalyst

X-Ray diffraction (XRD) patterns of pristine and U-BiNbO₄ indicate the presence of a multi-crystalline structure with orthorhombic and triclinic phases as shown in Fig. 2. The BiNbO₄ catalyst lattice parameters are *a* = 7.59 Å, *b* = 5.48 Å, and *c* = 7.95 Å. The U-BiNbO₄ lattice parameters are *a* = 7.52 Å, *b* = 5.39 Å, and *c* = 7.91 Å. The corresponding peaks are denoted with O for orthorhombic and T for triclinic, respectively (the space group is *P*1). Notably, the (121) and (040) triclinic peaks exhibit a shift to a higher angle from 28.01° and 30.36° for pristine BiNbO₄ to 28.20° and 30.49° for U-BiNbO₄, respectively. The decrease in lattice parameters can be ascribed to the carbon influence (from a urea source) leading to oxygen vacancies.[15,18] Since the ionic radius of O^{2-} is larger than the ionic radius of C^{4+} (126 pm and 30 pm, respectively),[27,28] the lattice shrinks due to the formation of oxygen vacancies (even after considering the volume expansion resulting from the interstitial carbon dopant). A larger peak shift was observed for the (121) *versus* (040) facet (0.188° *versus* 0.127°, respectively). This is evidence of the larger number of oxygen vacancies presented along (121) than the (040) facet, which can potentially contribute to a more pronounced photocatalytic activity of U-BiNbO₄. Compared to the pristine BiNbO₄, the U-BiNbO₄ does not exhibit the (031) triclinic peak and small peak ascribed to the Bi_2O_3 phase. In summary, the XRD results suggest that carbon doping occurs along the (121) and (040) planes.

X-Ray photoelectron spectroscopy (XPS) analysis was carried out to determine the chemical states existing in BiNbO₄ and U-BiNbO₄. Fig. 3 displays C1s and O1s chemical states for pristine BiNbO₄ and U-BiNbO₄, respectively. The curve fitting analysis of the C1s spectrum affords three major peaks at 284.6, 286.5 eV and 288.0 eV for pristine BiNbO₄, and
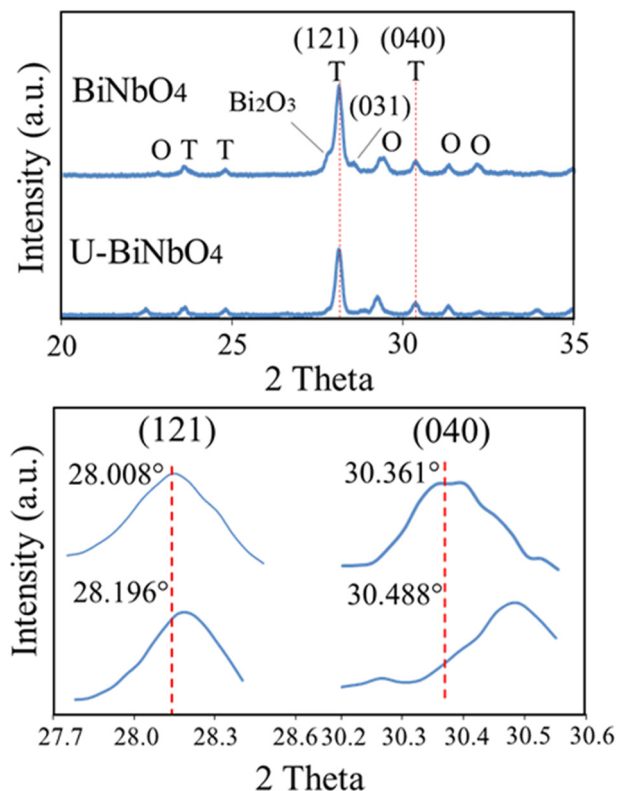
Fig. 2 XRD profiles for pristine $BiNbO_4$ and $U-BiNbO_4$, respectively. Bottom panel displays (121) and (040) triclinic peaks shift to a higher angle when urea is introduced.

284.6 eV, 286.3 eV and 288.1 eV for $U-BiNbO_4$, respectively. The peak at 284.6 eV originates from adventitious carbon, while the peaks at 286.3 eV and 288.1 eV are attributed to the C–O and C=O bonds, respectively.[16] Compared to pristine $BiNbO_4$, the C1s peaks of $U-BiNbO_4$ are shifted, indicating a different chemical environment, which is due to C doping. The presence

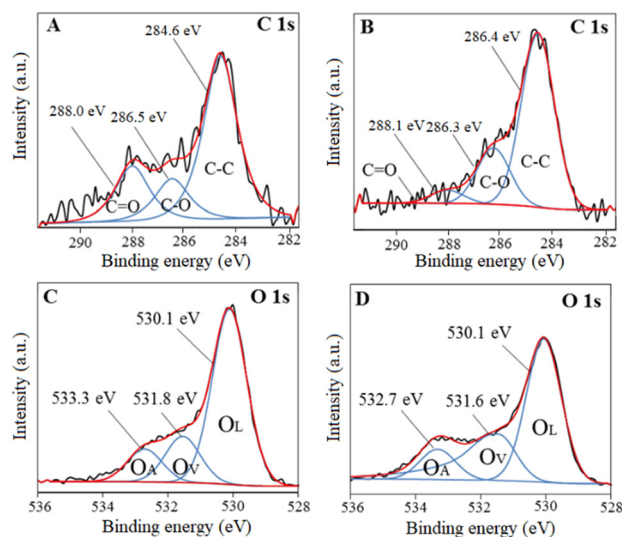Fig. 3 XPS spectra of C1s and O1s for pristine $BiNbO_4$ (panels A and C) and $U-BiNbO_4$ (panels B and D), respectively.

of surface carbon for $BiNbO_4$ and $U-BiNbO_4$ is 25.25 atomic% and 31.12 atomic%, respectively. The O1s peak was fitted into three components at 530.1 eV, 531.8 eV and 533.3 eV for pristine $BiNbO_4$ and 530.1 eV, 531.6 eV and 532.7 eV for $U-BiNbO_4$, respectively. These peaks were ascribed to lattice oxygen (OL), the region of surface oxygen vacancy (OV) and chemisorbed oxygen species (OA), respectively,[29,30] while the signal at 531.6 eV is also attributed to surface hydroxyls. The ratios of surface oxygen vacancies to the total oxygen are 8.60 atomic% and 8.84 atomic% for pristine $BiNbO_4$ and $U-BiNbO_4$, respectively. Oxygen vacancies were probed further using Raman spectroscopy (Fig. S1 in the ESI†). When compared to pristine $BiNbO_4$, the Raman active modes of $U-BiNbO_4$ shifted and broadened somewhat to a higher wavenumber, which is compatible with the reported observations of oxygen vacancies.[31] The formation of oxygen vacancies was further confirmed by using Raman spectroscopy. Therefore, it further confirmed the role of C doping in $BiNbO_4$.

The XPS spectrum of Bi4f and Nb3d for pristine $BiNbO_4$ and $U-BiNbO_4$ catalysts are shown in Fig. S2 in the ESI.† In summary, the elemental composition of $BiNbO_4$ is 25.25% of C, 44.02% of O, 14.59% of Bi and 14.05% of Nb. The elemental composition of $U-BiNbO_4$ is 31.12% of C, 48.56% of O, 8.04% of Bi and 17.7% of Nb. Enhancement of surface C and O atomic percentages were further validated by EDS elemental mapping as shown in Fig. S3 (in the ESI†) in which samples were deposited on top of a piece of Cu foil for the characterization to avoid C conductive adhesive. The presence of surface carbon for $BiNbO_4$ and $U-BiNbO_4$ is 25.40 atomic% and 38.30 atomic% and oxygen for $BiNbO_4$ and $U-BiNbO_4$ is 45.40 atomic% and 36.5 atomic%, respectively. As a result, it was established that urea doping increases carbon concentration, which was further demonstrated by an increase of C% in CHNS analysis, which can be seen from Table S1 (in the ESI†), in the XPS survey spectra (Fig. S4, ESI†) and has been explained thoroughly by Chaudhari et al.[32] This proves that urea reaction significantly contributed for C doping and contribution for N doping is negligible.
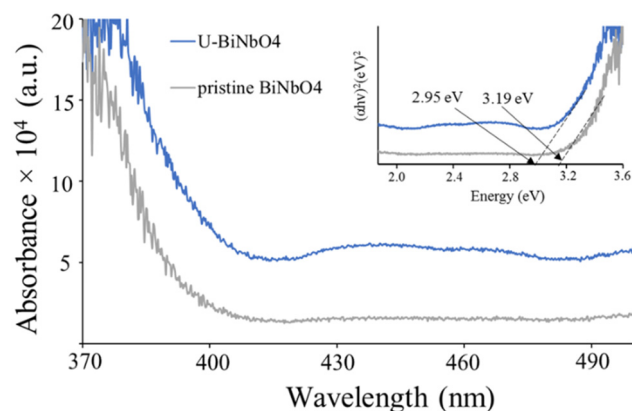

Fig. 4 UV-Vis absorbance spectroscopy of pristine $BiNbO_4$ and $U-BiNbO_4$. The inset of the plot shows band gap values from the corresponding Kubelka–Munk plot of pristine $BiNbO_4$ and $U-BiNbO_4$.
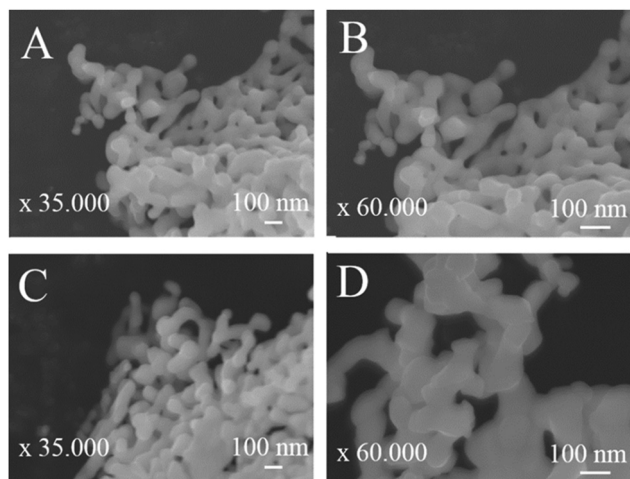
Fig. 5 SEM representative images of pristine $BiNbO_4$ (panels A and B) and U–$BiNbO_4$ (panels C and D).

Fig. 4 shows the absorbance spectra and the corresponding Kubelka–Munk plot (inset) of U-$BiNbO_4$ and pristine $BiNbO_4$. The band gap was found by extrapolating the linear portion of the absorption edge to the energy (eV) axis. The values were determined to be 2.95 eV and 3.19 eV for U-$BiNbO_4$ and pristine $BiNbO_4$, respectively. The reduced bandgap of U-$BiNbO_4$ is attributed to the presence of oxygen vacancies as it makes it easier to transport electrons from the valence band to the conduction band. The morphology and size of pristine and U-$BiNbO_4$ catalysts were examined using a Scanning Electron Microscope (SEM) and are shown in Fig. 5. Noticeably, the morphology and particle size do not differ much for doped and pristine samples with a sheet-like form of 200–400 nm in size. Additionally, slight agglomeration was observed leading to a larger structure of a few micrometers.

Photocatalytic degradation of methylene blue (MB) and brilliant green (BG) under visible light

Fig. 6 shows photocatalytic degradation of MB and BG dyes in the presence of pristine $BiNbO_4$ and U-$BiNbO_4$ under visible light irradiation. The solution pH at which the degradation reaction was carried out was pH = 11.5 in MB and pH = 11.3 in BG. The absorbance decay as a function of wavelength for MB and BG in the presence of U-$BiNbO_4$ is shown in Fig. S5 (in the ESI†). The light intensity was kept at 1 sun (100 mW cm^{-2}) and the kinetics was monitored using a UV-Vis technique. The total degradation time was set for 240 min with every 60 min period when the absorption properties of the suspension were evaluated. See Table 1 for a comparison to earlier efforts. The average and standard deviation values were based on n = 3 trials.

The best degradation rate of MB was ascribed to U-$BiNbO_4$ (75.7 ± 3.5%), followed by pristine $BiNbO_4$ (49.0 ± 2.6%). In aqueous solution MB shows a maximum absorption peak at 664 nm and a shoulder peak at 615 nm, which correspond to monomers and dimers, respectively.[33] Throughout the degradation both peaks exhibited a slight shift toward the blue region which is evidence of the N-demethylation reaction.[33,34]
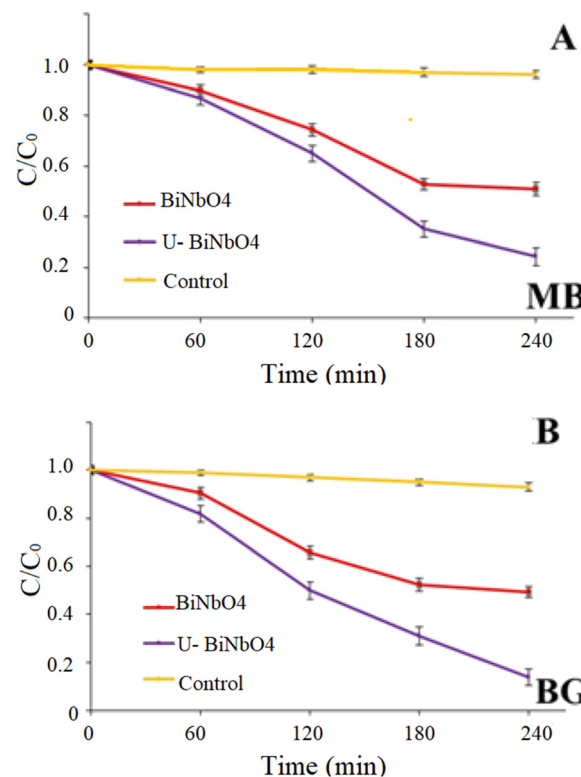

Fig. 6 Photocatalytic degradation and first-order kinetic plots of MB and BG dyes by pristine $BiNbO_4$ and U-$BiNbO_4$ under visible light.

The best BG removal rate was also attributed to U-$BiNbO_4$ (86.3 ± 3.5%), followed by pristine $BiNbO_4$ (51.0 ± 2.3%). The main peak is located at 619 nm and showed a gradual decrease within 240 min. The decay was accompanied by a noticeable hypsochromic shift toward the blue region (from 619 nm to 603 nm) proving the N-demethylation degradation pathway, which is shown in Fig. S5 in the ESI.†

Fig. S6 (in the ESI†) represents the degradation rates of MB and BG against different amounts of U-$BiNbO_4$ catalyst. The amount was varied from 10 to 45 mg, and the irradiation time was set for 240 min. It can be seen that for MB the best decomposition rate was ascribed to 10 and 15 mg of the catalyst (49.6 ± 2.6% and 75.7 ± 3.5%, respectively). With higher catalyst loading the degradation rate drastically drops to 28.8 ± 2.0% and 15.1 ± 1.7% for 30 and 45 mg, respectively. BG degrades rapidly in the presence of 15 mg of catalyst (86.3 ± 2.9%), followed by 30 and 45 mg (67.2 ± 2.8% and 63.7 ± 2.5%, respectively). Higher loading and the accompanying drop in degradation efficiency can be explained by particle–particle interactions. When the number of particles in the system increases, it causes the formation of a higher number of free radicals participating in the dye degradation process. At the same time, beyond a certain limit of catalyst amount, the turbidity of the solution prevents visible light from penetrating and decreases the overall efficiency in the catalytic system.[35]

In order to identify the degradation mechanism of MB and BG dyes in the presence of U-$BiNbO_4$, hydroxyl radicals (•OH), electron and hole scavenging experiments were executed and
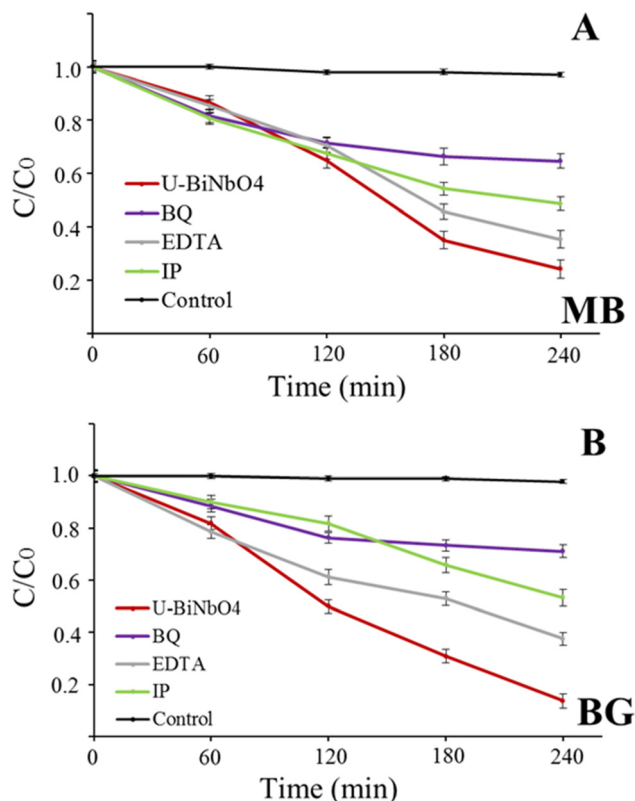
Fig. 7 Photocatalytic degradation with the U-BiNbO$_4$ catalyst in the presence of carrier scavengers (BQ, EDTA, IP) for (A) MB and (B) BG.

the results are shown in Fig. 7. EDTA, *p*-benzoquinone (BQ), and isopropanol (IP) were used to scavenge holes, electrons and $^\bullet$OH radicals, respectively. For both dyes the reaction kinetics significantly decreased in the presence of BQ, highlighting the dominant role of electrons in the degradation process (35.3 ± 2.6% for MB and 28.8 ± 2.4% for BG, respectively). The hydroxyl radical is another important specie that affects the degradation rate (51.3 ± 2.6% for MB and 46.6 ± 3.2% for BG, respectively), while holes participate the least in the degradation process.

Proposed mechanism of photocatalytic activity

The values of the valence band (VB) and the conduction band (CB) can be found from the measured band gap of U-BiNbO$_4$ (E_g = 2.95 eV), the electronegativity of the catalyst (χ = 6.26 eV)[34] and the parameter relating the reference of the electrode's redox level to the absolute vacuum scale (E_0 = 4.5 eV). The following empirical eqn (1) and (2) can be used:

$$E_{VB} = X - E_0 + 0.5\, E_g \qquad (1)$$

$$E_{CB} = E_{VB} - E_g \qquad (2)$$

Based on the above parameters, the values of VB and CB *vs.* NHE are 3.235 eV and 0.285 eV, respectively. The schematic photocatalytic mechanism of MB and BG degradation is shown in Fig. 8. Based on the scavenging experiments from Fig. 7, photoelectrons are the primary reactive species affecting the degradation process, followed
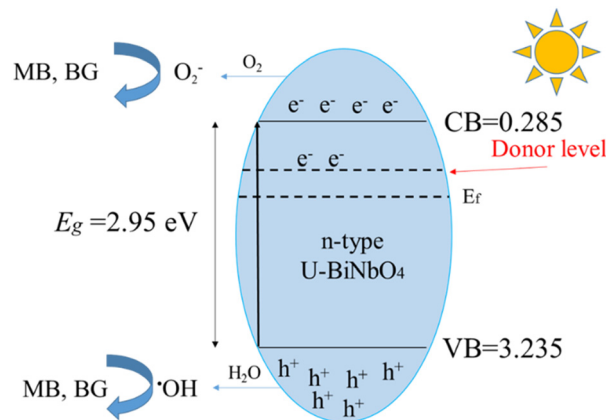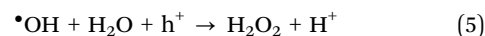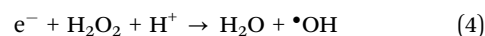

Fig. 8 Schematic photocatalytic mechanism of MB and BG degradation.

by $^\bullet$OH radicals and photo-holes. The proposed sequence of chemical reactions is the following:[13,16,25,36]

$$U\text{-BiNbO}_4 + h\nu \rightarrow U\text{-BiNbO}_4 + e^- + h^+ \qquad (3)$$

$$e^- + H_2O_2 + H^+ \rightarrow H_2O + {}^\bullet OH \qquad (4)$$

$${}^\bullet OH + H_2O + h^+ \rightarrow H_2O_2 + H^+ \qquad (5)$$

The enhanced photocatalytic properties of U-BiNbO$_4$ can be ascribed to the cumulative effect of carbon doping and oxygen vacancies.[37] As the band gap of U-BiNbO$_4$ (compared to pristine BiNbO$_4$) reduced, the electrical resistivity drops. Additionally, the increased amount of oxygen vacancies makes U-BiNbO$_4$ a more efficient n-type semiconductor, acting as an electron donor, and helping to inhibit electron–hole recombination.[9,16] Secondly, doping with carbon changes the flat potential of U-BiNbO$_4$, leading to the formation of a potential barrier.[16] The potential barrier yields transfer of photoelectrons to carbon species, promoting electron–hole separation. At the next stage, hydrogen at the surface of the catalyst reacts with photoelectrons to produce hydroxyl radicals ($^\bullet$OH, from reaction (4). Photo-holes react with water and $^\bullet$OH, yielding a large amount of H$_2$O$_2$ (from reaction (5)). Thus, degradation of MB and BG dyes is the combination of photocatalytic (by photoelectrons and photo-holes) and photo-oxidative (by $^\bullet$OH and H$_2$O$_2$) pathways.

However, the effects of semiconductor band gaps, band edge positions (as reported by R. Yang *et al.* for carbon-doped BiVO$_4$[37]), and photogenerated electron–hole pair recombination rates on the generation rates of the aforementioned active radicals have not yet been thoroughly investigated. In order to forecast charge transport in photoelectrochemical systems that incorporate electrode entropy, electrolyte chemistry and electronic structures, our team is now extending its existing charge transport prediction models for general electrochemical cells to photo-electrochemical systems.[38]

Conclusions

In this work we employed urea-assisted synthesis to prepare a carbon-doped BiNbO$_4$ catalyst *via* a facile sol–gel method.

This approach has been previously shown only for TiO_2 and ZnO.[15,16] Gaseous ammonia, which originated from the thermal decomposition of urea, allowed us to apply a combination of oxygen-poor (300–400 °C) and oxygen-rich atmospheres (below 300 °C and above 400 °C). The unique synthesis conditions lead to (1) enhanced presence of carbon (from 25.25 atomic% for pristine $BiNbO_4$ to 31.12 atomic% for U-$BiNbO_4$) and (2) enhanced presence of oxygen vacancies (from 8.60 atomic% for pristine $BiNbO_4$ to 8.84 atomic% for U-$BiNbO_4$). Tuned properties of the U-$BiNbO_4$ catalyst resulted in superior properties toward the degradation of cationic MB and BG pollutants under visible light (75.7 ± 3.5% and 86.3 ± 3.5% after 4 hours, respectively). The excellent photocatalytic performance was ascribed to the role of carbon and the resultant oxygen vacancies by promoting electron–hole separation. Based on carrier scavenger experiments, photoelectrons are the major species affecting degradation kinetics, followed by $^{\bullet}OH$ radicals and photo-holes. The combination of oxygen-rich and oxygen-poor atmospheres can be an effective tool to enhance the photocatalytic properties of Bi-based catalysts.

Author contributions

The manuscript was written through contributions of all authors. All authors have given approval to the final version of the manuscript.

Conflicts of interest

The authors declare no conflict of interest.

Acknowledgements

References

1 S. Akel, R. Dillert, N. O. Balayeva, R. Boughaled, J. Koch, M. El Azzouzi and D. W. Bahnemann, *Catalysts*, 2018, **8**, 647.

2 M. Bakiro, S. H. Ahmed and A. Alzamly, *J. Environ. Chem. Eng.*, 2020, **8**, 104461.

3 S. S. Dunkle and K. S. Suslick, *J. Phys. Chem. C*, 2009, **113**, 10341–10345.

4 S. Xiong, Y. Liu, T. Li, F. Li and W. Cao, *Ceram. Int.*, 2020, **46**, 21790–21793.

5 H.-F. Zhai, A.-D. Li, J.-Z. Kong, X.-F. Li, J. Zhao, B.-L. Guo, J. Yin, Z.-S. Li and D. Wu, *J. Solid State Chem.*, 2013, **202**, 6–14.

6 J. Zhao, Q. He, X. Zhang, J. Yang, B. Yao, Q. Zhang and X. Yu, *Integr. Ferroelectr.*, 2016, **176**, 37–53.

7 N. Zhuk, S. Shugurov, M. Krzhizhanovskaya, V. Belyy, N. Sekushin, B. Makeev, S. Nekipelov, D. Beznosikov and Y. A. Busargina, *J. Alloys Compd.*, 2020, **822**, 153619.

8 Q.-C. Cao, X.-B. Ding, F. Li, Y.-H. Qin and C. Wang, *J. Colloid Interface Sci.*, 2020, **576**, 139–146.

9 S. Cho, J.-W. Jang, J. S. Lee and K.-H. Lee, *CrystEngComm*, 2010, **12**, 3929–3935.

10 V. M. Naik, D. B. Gunjal, A. H. Gore, S. P. Pawar, S. T. Mahanwar, P. V. Anbhule and G. B. Kolekar, *Diamond Relat. Mater.*, 2018, **88**, 262–268.

11 Y. Shi, G. Liu, L. Wang and H. Zhang, *J. Colloid Interface Sci.*, 2019, **557**, 336–348.

12 G. Sun, L. Ma, J. Ran, B. Li, X. Shen and H. Tong, *Electrochim. Acta*, 2016, **194**, 168–178.

13 X. Wu, S. Yin, Q. Dong, C. Guo, H. Li, T. Kimura and T. Sato, *Appl. Catal., B*, 2013, **142**, 450–457.

14 Y. Yang, D. Ni, Y. Yao, Y. Zhong, Y. Ma and J. Yao, *RSC Adv.*, 2015, **5**, 93635–93643.

15 C. Di Valentin, G. Pacchioni and A. Selloni, *Chem. Mater.*, 2005, **17**, 6656–6665.

16 J. Lu, Y. Wang, J. Huang, J. Fei, L. Cao and C. Li, *Dyes Pigm.*, 2017, **144**, 203–211.

17 K. Mallikarjuna, G. A. R. Bari, S. P. Vattikuti and H. Kim, *Int. J. Hydrogen Energy*, 2020, **45**, 32789–32796.

18 X. Zhang, J. Qin, R. Hao, L. Wang, X. Shen, R. Yu, S. Limpanart, M. Ma and R. Liu, *J. Phys. Chem. C*, 2015, **119**, 20544–20554.

19 S. T. Tan, X. Sun, Z. Yu, P. Wu, G. Q. Lo and D. L. Kwong, *Appl. Phys. Lett.*, 2007, **91**, 072101.

20 W.-J. Yin, S.-H. Wei, M. M. Al-Jassim, J. Turner and Y. Yan, *Phys. Rev. B: Condens. Matter Mater. Phys.*, 2011, **83**, 155102.

21 J. Liu, T. Zhang, Z. Wang, G. Dawson and W. Chen, *J. Mater. Chem.*, 2011, **21**, 14398–14401.

22 F. Dong, L. Wu, Y. Sun, M. Fu, Z. Wu and S. Lee, *J. Mater. Chem.*, 2011, **21**, 15171–15174.

23 Y. Zhang, J. Liu, G. Wu and W. Chen, *Nanoscale*, 2012, **4**, 5300–5303.

24 N. Li, S. Miao, X. Zheng, J. Lai, S. Lv, X. Gu, M. Zhang, J. Yang and S. Cui, *Ceram. Int.*, 2019, **45**, 24260–24268.

25 A. Lebedev, F. Anariba, X. Li, D. Seng Hwee Leng and P. Wu, *Sol. Energy*, 2019, **178**, 257–267.

26 J. Hao, Q. Wang and Z. Zhao, *J. Photochem. Photobiol., A*, 2017, **335**, 94–101.

27 E. Keve and A. Skapski, *J. Solid State Chem.*, 1973, **8**, 159–165.

28 R. Shannon, *Acta Crystallogr., Sect. A: Cryst. Phys., Diffr., Theor. Gen. Crystallogr.*, 1976, **32**, 751–767.

29 D. Li, W. Wang, D. Jiang, Y. Zheng and X. Li, *RSC Adv.*, 2015, **5**, 14374–14381.

30 J.-M. Wu, Y. Chen, L. Pan, P. Wang, Y. Cui, D. Kong, L. Wang, X. Zhang and J.-J. Zou, *Appl. Catal., B*, 2018, **221**, 187–195.

31 H. Mai, T. Lu, Q. Sun, J. Langley, N. Cox, F. Kremer, K. Catchpole, H. Chen, Z. Yi and T. J. Frankcombe, *J. Mater. Chem. A*, 2021, **9**, 13182–13191.

32 N. K. Chaudhari, M. Y. Song and J.-S. Yu, *Sci. Rep.*, 2014, **4**, 1–10.

33 R. Zuo, G. Du, W. Zhang, L. Liu, Y. Liu, L. Mei and Z. Li, *Adv. Mater. Sci. Eng.*, 2014, **2014**, 7.

34 F. Wang, S. Min, Y. Han and L. Feng, *Superlattices Microstruct.*, 2010, **48**, 170–180.

35 A. Kumar, *A Review on the Factors Affecting the Photocatalytic Degradation of Hazardous Materials*, 2017.

36 A. Lebedev, G. H.-H. Ma, F. Anariba, X. Li, T. S. K. Lim, F. C. Ng and P. Wu, *Sol. Energy*, 2018, **160**, 298–302.

37 R. Yang, R. Zhu, Y. Fan, L. Hu and Q. Chen, *RSC Adv.*, 2019, **9**, 14004–14010.

38 P. Wu and H. L. Senevirathna, *Electrochim. Acta*, 2022, **410**, 140051.